 CMC, vol.19, no.3, pp.255-284, 2010

Numerical Analysis of Large Strain Simple Shear and Fixed-End Torsion of HCP Polycrystals

H. Wang[1], Y. Wu[2], P.D. Wu[1] and K.W. Neale[3]

Abstract: Large strain homogeneous simple shear of Hexagonal Close Packed (HCP) polycrystals is first studied numerically. The analyses are based on the classical Taylor model and the Visco-Plastic Self-Consistent (VPSC) model with various Self-Consistent Schemes (SCSs). In these polycrystal plasticity models, both slip and twinning contribute to plastic deformations. The simple shear results are then extended to the case of solid circular bars under large strain fixed-end torsion, where it is assumed that the solid bar has the same mechanical properties as the element analyzed for large strain simple shear. It is shown that the predicted second-order axial force is very sensitive to the initial texture, texture evolution and the constitutive models employed. Numerical results suggest that the torsion test can provide an effective means for assessing the adequacy of polycrystal plasticity models for HCP polycrystalline materials.

Keywords: Torsion, Magnesium, Twinning; Swift effect, Texture.

1 Introduction

As a material with low density, magnesium and its alloys have been increasingly used for automotive, aeronautical and aerospace parts and structures. Magnesium alloys are of Hexagonal Close Packed (HCP) crystallographic structure with low symmetry and consequently exhibit high anisotropy in mechanical behavior. The plastic deformation in most Face Centered Cubic (FCC) and Body Centered Cubic (BCC) is dominated by crystallographic slip. In contrast, both slip and twinning contribute to the plastic deformation in HCP crystals. At the crystal level, the constitutive modeling for HCP single crystals is much more complicated than that for

[1] Department of Mechanical Engineering, McMaster University, Hamilton, Ontario L8S 4L7, Canada

[2] State Key Laboratory for Geomechanics and Deep Underground Engineering, China University of Mining and Technology, Xuzhou, Jiangsu 221008, China.

[3] Faculty of Engineering, University of Sherbrooke, Sherbrooke, Quebec J1K 2R1, Canada

FCC and BCC crystals. The reasons for this are (1) twinning must be accounted for in HCP crystals; and (2) different types of slip systems exist in HCP crystals, although very few slip systems can be activated at room temperature. At the polycrystal level, compared to the constitutive modeling for FCC and BCC polycrystals, additional difficulty in the constitutive modeling for HCP polycrystals is that interactions between crystals/grains are much more significant due to low crystallographic symmetry; these must be carefully considered.

Among the various polycrystal plasticity models, the classical Taylor (1938) model has been the most popular one. The Taylor model, known as the upper bound model, assumes that all grains must accommodate the same plastic strain, equal to the macroscopically imposed strain. In this model, the actual heterogeneities that occur during the deformation of polycrystals are neglected. More specifically, the Taylor model neglects strain variations from grain to grain in the polycrystalline aggregate. The Taylor model has played an important role in the field of sheet metal forming (see, e.g., Dawson et al., 2003; Wu et al., 1997). Noticeable new advance in the Taylor polycrystal plasticity model has been the incorporation of deformation twinning (see e.g. Kalidindi, 1998; Staroselsky and Anand, 1998, 2003; Wu *et al.*, 2007a). Another popular type of polycrystal plasticity model is based on the self-consistent approach, originally proposed by Kröner (1958). In general, self-consistent models assume that each grain is an ellipsoidal inclusion embedded in an infinite homogeneous equivalent medium (HEM). The consistency conditions require that the averaged behavior over all the grains must be the same as the macroscopically imposed one. Since stress and strain variations from grain to grain and interactions among grains in an HCP polycrystalline aggregate are significant and cannot be neglected in an attempt to accurately describe the deformation, it is expected that a self-consistent approach may be more suitable than the full constraint Taylor approach for the constitutive modeling of HCP polycrystals. Among the various self-consistent plasticity models, the Visco-Plastic Self-Consistent (VPSC) model developed by Molinari et al. (1987) and Lebensohn and Tomé (1993, 1994) has been widely used to simulate the large strain behavior and texture evolution of HCP polycrystalline Mg under various deformations (see e.g. Agnew and Duygulu, 2005; Jain and Agnew, 2007; Xu et al., 2008). Recently, Wang et al. (2010a) have developed a finite strain elastic-viscoplastic self-consistent model (EVPSC) for polycrystalline materials. The EVPSC model is a completely general elastic-viscoplastic, fully anisotropic, self-consistent polycrystal model, applicable at large strains and to any crystal symmetry. However, it has been found that numerical results are extremely sensitive to the Self-Consistent Schemes (SCSs) applied even when the values of the material constants are assumed to be the same for various SCSs (see e.g. Wang et al., 2010a). Therefore, it is necessary to carry out an assess-

ment of the predictive capability of the VPSC/EVPSC model with various SCSs. Wang et al. (2010b) numerically studied the large strain behavior of magnesium alloy AZ31B sheet under uniaxial tension and compression along different directions. An assessment of the predictive capability of the polycrystal plasticity models was made based on comparisons of the predicted and experimental stress responses and R values. While Wang et al. (2010b) performed the evaluation based on deformation processes that do not involve significant shear; the present paper intends to further evaluate various SCSs by studying large strain homogeneous simple shear and fixed-end torsion of HCP polycrystals.

Focusing on large strain torsion, the present study is motivated by the fact that the torsion test provides an excellent means for obtaining experimental data for the constitutive behavior of elastic-plastic solids at large to very large deformations. The advantage over the standard tensile test is that deformations of a solid bar in torsion remain axially homogeneous up to final failure without giving rise to strain localization phenomena such as necking and shear banding. Evidently, torsional deformations are inhomogeneous in the radial direction, but this multiaxiality is lower and more tractable than the three-dimensional state inside necks, etc. Furthermore, it is well-known that the axial stress development during fixed-end torsion and the axial elongation during free-end torsion in initially isotropic polycrystalline metals are mainly due to texture development (Montheillet et al., 1984; Toth et al., 1992). The predictions of these second-order axial effects, often called the "Swift effect" (Swift, 1947), depend strongly on the constitutive model – in particular on the description of anisotropic hardening (see, e.g., Harren et al., 1989; Wu et al., 1996). Thus, the torsion test seems to provide an effective means for assessing the adequacy of proposed constitutive models. It has been found that the axial effect is more pronounced in thin-walled tubes than in solid bars (see e.g. Billington, 1977). In fact, many experimental procedures based on torsion have used thin-walled tubes for which the state of the deformation has been assumed to be completely uniform and, for fixed-end torsion, to be a state of simple shear (Field and Adams, 1990). Reducing the wall thickness of a tube will reduce the nonuniformity of the deformation and, if the tubes are extremely thin, then the deformation can be approximated to be homogeneous so that the experimental results can be easily interpreted. Unfortunately, in order to avoid buckling in a finite deformation torsion experiment on a hollow tube, it is necessary that the thickness of the tube be at least 10-15% of the mean radius (Khen and Rubin, 1992). Based on a detailed finite element analysis Wu and Van der Giessen (1993) have found that these hollow tubes cannot really be considered to be thin and the deformation is not really homogeneous. In addition to this, a thin hollow tube is much more difficult to manufacture and grip than a solid bar so that, in view of the various experimental problems, thin-walled

tubes seem to be of less practical importance at large strains. Consequently, the numerical simulation of solid bars under large-strain torsion, accounting accurately for nonuniform states of deformation, is of considerable practical significance.

Obviously, the torsion test on a solid circular bar involves stress and deformation gradients along the radius of the bar, as well as non-proportional stressing histories and rotations of the principal axes of strain for each element of the cross-section. Therefore, the analysis of large strain solid bar torsion is considerably more involved. Fortunately, Neale and Shrivastava (1985, 1990) have found that if the behavior is axisymmetric, axially homogeneous and incompressible, semi-analytical solutions can be obtained for solid bars subjected to fixed-end torsion. Neale et al. (1990) have applied the method to study the fixed-end torsion of a solid bar using a rigid plastic version of the Taylor polycrystal model. In the present paper, this semi-analytical approach is used to simulate large strain torsion of solid bars of HCP polycrystals under fixed-end conditions.

Although extensive experimental and numerical research has been performed on large strain torsion for FCC and BCC polycrystals, there are rare investigations on the torsion of HCP materials. Sanchez et al. (2001) and Evans et al. (2005) studied texture evolution during torsion by simulating simple shear. Barnett (2001) experimentally studied the flow stress of AZ31 under torsion. Balasubramanian and Anand (2002) numerically studied texture evolution and the mechanical response of titanium under fixed-end torsion of a circular tube by using the finite element method. Very recently, Beausir et al. (2009) experimentally and numerically studied the free-end torsion of AZ71 and pure Mg. To the best of our knowledge, however, all the numerical studies on the large strain torsion of HCP polycrystals have excluded twinning.

In this paper, we numerically study the large strain simple shear and fixed-end torsion of HCP polycrystals. All the simulations are based on the classical Taylor model and the VPSC model with various SCSs. In these polycrystal plasticity models both slip and twinning contribute to plastic deformations in HCP polycrystals. The plan of this paper is as follows. In Section 2, the fixed-end torsion problem formulation and the method of solution are presented. In Section 3, we briefly review the constitutive models. We begin Section 4 by showing two initial textures and listing values of the material parameters in the Taylor and VPSC analyses with various SCSs. These values of the material parameters are then used to predict large strain behavior under simple shear and fixed-end torsion. Differences in predictions between the various models are emphasized. The conclusion is presented in Section 5.

2 Problem formulation and method of solution

We consider an incompressible solid circular bar with radius R and length L subjected to an angle of twist ψ (Fig. 1). The bar is assumed to be constrained axially, thus allowing the possible development of axial stresses and a resultant axial force F. The end faces of the bar are constrained to the extent that they remain plane and perpendicular to the axial direction, so that we may assume that any cross-section of the bar remains planar. The lateral surface of the bar is stress free, and all properties are assumed to be axisymmetric and homogeneous along the axial direction. Although anisotropy will be induced during the deformation process, the behavior remains axisymmetric and the bar remains circular cylindrical.

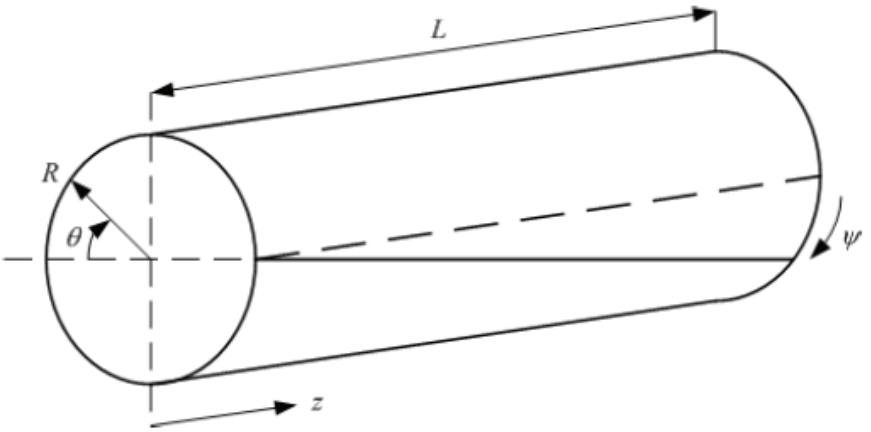

Figure 1: Schematic representation of an axially-constrained solid circular bar under torsion.

The kinematics of the problem is readily determined with the aid of a spatial fixed cylindrical polar coordinate system $x^i = (r, \theta, z)$ with orthonormal base vectors $\mathbf{e}_1 = \mathbf{e}_r$, $\mathbf{e}_2 = \mathbf{e}_\theta$, $\mathbf{e}_3 = \mathbf{e}_z$. These base vectors are associated with material elements in their current, deformed state so that physical components are represented by tensor components with respect to this basis. If the initial, undeformed coordinates of a material point are (r, θ_0, z), its current, deformed coordinates are given by (r, θ, z) with $\theta = \theta_0 + (z/L)\psi$. Accordingly, the velocity gradient tensor $\mathbf{l} = l_{ij}\mathbf{e}_i\mathbf{e}_j$ is

$$[l_{ij}] = \begin{bmatrix} 0 & 0 & 0 \\ 0 & 0 & \dot{\gamma} \\ 0 & 0 & 0 \end{bmatrix} \tag{1}$$

where $\dot{\gamma} = \dot{\psi}(r/L)$. Thus, each element of the bar is in a state of simple shear in the $\theta - z$ plane, where the shear deformation γ is directly proportional to the radial distance r. That is,

$$\gamma(r) = \frac{r}{R}\Gamma \tag{2}$$

where $\Gamma = \psi(R/L)$ represents the shear strain at the outer radius of the bar.

With the hypothesis that the behavior is axisymmetric, axially homogeneous and incompressible, Neale and Shrivastava (1990) have developed the semi-analytical solutions for solid bars subjected to fixed-end torsion. Their approach is based on the observation that each material element is simply loaded in simple shear under an additional hydrostatic pressure, where the shear strain γ is directly proportional to the radius r, as shown in (1) and (2). To apply this semi-analytical method, the quantities of the deviatoric stress components s_{ij} during simple shear are required as a function of the shear deformation γ, which is then readily translated into the deviatoric stress distribution $s_{ij}(r)$. The Cauchy stress distribution $\sigma_{ij} = s_{ij} - p\delta_{ij}$ (where δ_{ij} is Kronecker delta) is obtained when the hydrostatic pressure distribution $p(r)$ is found.

Because of axisymmetry and the prescribed boundary conditions, we have $\sigma_{r\theta} = \sigma_{rz} = 0$ throughout the bar. The only equation of equilibrium which is not identically satisfied is the relation

$$r\frac{\mathrm{d}\sigma_{rr}}{\mathrm{d}r} + \sigma_{rr} - \sigma_{\theta\theta} = 0 \tag{3}$$

This can be written in terms of p and the known stress deviator distribution $s_{ij}(r)$ as follows

$$\frac{\mathrm{d}p}{\mathrm{d}r} = \frac{\mathrm{d}s_{rr}}{\mathrm{d}r} + \frac{1}{r}(s_{rr} - s_{\theta\theta}) \tag{4}$$

With the boundary condition $\sigma_{rr}(R) = 0$, equation (4) can be integrated to give the hydrostatic pressure distribution $p(r)$

$$p(r) = s_{rr} - \int_r^R \frac{1}{r}(s_{rr} - s_{\theta\theta})dr \tag{5}$$

Combining the pressure $p(r)$ with the previously determined stress deviator distributions $s_{ij}(r)$ gives the Cauchy stress distributions $\sigma_{ij}(r)$. The resultant torque T and axial force F are given by

$$\begin{aligned} T(\Gamma) &= 2\pi \int_0^R r^2 \sigma_{z\theta} dr \\ F(\Gamma) &= 2\pi \int_0^R r\sigma_{zz} dr \end{aligned} \tag{6}$$

It is clear that the hydrostatic pressure has no influence on T since $\sigma_{z\theta} = s_{z\theta}$. Numerical results are presented in terms of the shear strain at the outer radius of the bar Γ , the mean shear stress $\bar{\tau}$ and mean axial stress $\bar{\sigma}$ in the bar defined by:

$$\Gamma = \psi \frac{R}{L},\ \bar{\tau} = \frac{3T}{2\pi R^3},\ \bar{\sigma} = \frac{F}{\pi R^2} \tag{7}$$

In summary, the deviatoric stress components s_{ij}, as functions of the shear strain γ in simple shear (in the $\theta - z$ plane) described by (1), are first calculated either analytically or numerically based on a constitutive model. Because the shear strain γ is directly proportional to the radial distance r according to (2), the calculated deviatoric stress components s_{ij} during simple shear are readily translated into the deviatoric stress distributions $s_{ij}(r)$ in torsion. The pressure distribution across the bar under torsion is computed by numerically integrating (5), and the Cauchy stress distributions $\sigma_{ij}(r)$ are then obtained through $\sigma_{ij} = s_{ij} - p\delta_{ij}$. Finally, the resultant axial force and torque are calculated by numerically integrating (6).

3 Polycrystal plasticity models

The plastic deformation of a crystal is assumed to be due to crystallographic slip and twinning on the slip and twinning systems $(\mathbf{s}^\alpha, \mathbf{n}^\alpha)$. Here, $\mathbf{s}^\alpha$ and $\mathbf{n}^\alpha$ are respectively the slip/twinning direction and normal direction of the slip/twinning system α in the present configuration. The following equation relates the grain (crystal) level plastic strain rate $\mathbf{d}^g$, and stress $\boldsymbol{\sigma}^g$ (see e.g. Asaro and Needleman, 1985):

$$\mathbf{d}^g = \sum_\alpha \dot{\gamma}^\alpha \mathbf{P}^\alpha \tag{8}$$

where $\dot{\gamma}^\alpha$ is the shear rate of slip (twinning) system α, and $\mathbf{P}^\alpha$ is the associated Schmid tensor:

$$\mathbf{P}^\alpha = \frac{1}{2}(\mathbf{s}^\alpha \mathbf{n}^\alpha + \mathbf{n}^\alpha \mathbf{s}^\alpha) \tag{9}$$

For slip,

$$\dot{\gamma}^\alpha = \dot{\gamma}_0 \left| \frac{\tau^\alpha}{\tau^\alpha_{cr}} \right|^{\frac{1}{m}} sgn(\tau^\alpha) \tag{10}$$

whereas, for twinning,

$$\begin{aligned} &\dot{\gamma}^\alpha = \dot{\gamma}_0 \left(\frac{\tau^\alpha}{\tau^\alpha_{cr}} \right)^{\frac{1}{m}} \text{ for } \tau^\alpha > 0 \\ &\dot{\gamma}^\alpha = 0 \text{ for } \tau^\alpha \leq 0 \end{aligned} \tag{11}$$

where $\dot{\gamma}_0$ is a reference value of slip/twinning rate, m is the slip/twinning rate sensitivity, and τ^α is the resolved shear stress:

$$\tau^\alpha = \boldsymbol{\sigma}^g : \mathbf{P}^\alpha \tag{12}$$

τ^α_{cr} is the critical resolved shear stress (CRSS), and sgn represents the sign function. The evolution of τ^α_{cr} is taken in the form of

$$\dot{\tau}^\alpha_{cr} = \frac{\mathrm{d}\hat{\tau}^\alpha}{\mathrm{d}\gamma_{ac}} \sum_\beta h^{\alpha\beta} \dot{\gamma}^\beta \tag{13}$$

where $\gamma_{ac} = \sum_\alpha \int |\dot{\gamma}^\alpha| \, dt$ is the accumulated shear strain in the grain, and $h^{\alpha\beta}$ is the latent hardening coupling coefficient which empirically accounts for the obstacles on system α associated with system β. If there are k crystallographically equivalent slip/twinning modes and the ith mode has n_i slip/twinning systems, we take $h^{\alpha\beta}$ in the form of

$$h^{\alpha\beta} = \begin{bmatrix} \mathbf{A}_{n_1\times n_1} & q_{12}\mathbf{A}_{n_1\times n_2} & \cdots & q_{1k}\mathbf{A}_{n_1\times n_k} \\ q_{21}\mathbf{A}_{n_2\times n_1} & \mathbf{A}_{n_2\times n_2} & \cdots & q_{2k}\mathbf{A}_{n_2\times n_k} \\ \vdots & \vdots & & \vdots \\ q_{k1}\mathbf{A}_{n_k\times n_1} & q_{k2}\mathbf{A}_{n_k\times n_2} & \cdots & \mathbf{A}_{n_k\times n_k} \end{bmatrix} \tag{14}$$

where q_{ij} is the ratio of the latent hardening rate of mode j to the self-hardening rate of mode i, and $\mathbf{A}_{n_i\times n_j}$ is an n_i by n_j matrix fully populated by ones (Wang et al., 2010c). $\hat{\tau}^\alpha$ is the threshold stress and is characterized by

$$\hat{\tau}^\alpha = \tau^\alpha_0 + (\tau^\alpha_1 + h^\alpha_1 \gamma_{ac}) \left(1 - \exp(-\frac{h^\alpha_0}{\tau^\alpha_1}\gamma_{ac})\right) \tag{15}$$

Here,τ_0, h_0, h_1 and $\tau_0 + \tau_1$ are the initial CRSS, the initial hardening rate, the asymptotic hardening rate, and the back-extrapolated CRSS, respectively.

Various homogenization methods have been developed to characterize the mechanical behavior of a polycrystalline aggregate from the responses of their single crystals. Among them, the most popular Taylor model assumes that the strains of each grain are equal to the imposed macroscopic strains, and the macroscopic stresses are the average of the stresses over all the grains. Another popular homogenization method is the self-consistent approach, which assumes each grain to be an ellipsoidal inclusion embedded in a homogeneous effective medium (HEM), which is the aggregate of the grains. The Eshelby inclusion formulism (Eshelby, 1957) is used to describe the interaction between each grain and the aggregate. During each

deformation step, the single crystal constitutive law, which describes the grain-level response, and the self-consistency criteria are solved simultaneously. This enables the grain-level stresses and strain rates to be consistent with the boundary conditions imposed on the surrounding polycrystalline aggregate.

The linearized behavior of inclusion (single crystal) can be written as

$$\mathbf{d}^g = \mathbf{M}^g : \boldsymbol{\sigma}^g + \mathbf{d}_0^g \tag{16}$$

where $\mathbf{M}^g$ and $\mathbf{d}_0^g$ are the visco-plastic compliance and the back-extrapolated term of grain g, respectively. The linearized behavior of the HEM (polycrystal) is analogous to the inclusion and is written as

$$\mathbf{D} = \bar{\mathbf{M}} : \boldsymbol{\sigma} + \mathbf{D}_0 \tag{17}$$

where $\bar{\mathbf{M}}$, $\mathbf{D}$, $\boldsymbol{\sigma}$ and $\mathbf{D}_0$ are the visco-plastic compliance, strain rate, stress and the back-extrapolated term of the HEM, respectively. The relation of grain-level stress and strain rate to the aggregate response is obtained self-consistently by

$$(\mathbf{d}^g - \mathbf{D}) = -\tilde{\mathbf{M}}^g : (\boldsymbol{\sigma}^g - \boldsymbol{\sigma}) \tag{18}$$

The interaction tensor $\tilde{\mathbf{M}}$ is calculated from

$$\tilde{\mathbf{M}}^g = (\mathbf{I} - \mathbf{S}^g)^{-1} : \mathbf{S}^g : \bar{\mathbf{M}} \tag{19}$$

where $\mathbf{S}^g$ is the Eshelby tensor for a given grain, and $\mathbf{I}$ is the identity tensor. Different SCSs depend on different choices of this linearization. The following linearization schemes are adopted in this paper:

(a) Secant:

$$\begin{aligned} M_{ijkl}^{g,\mathrm{sec}} &= \dot{\gamma}_0 \sum_\alpha \left(\frac{\tau^\alpha}{\tau_{cr}^\alpha} \right)^{\frac{1}{m}-1} \frac{P_{ij}^\alpha P_{kl}^\alpha}{\tau_{cr}^\alpha} \\ d_{0ij}^{g,\mathrm{sec}} &= 0 \end{aligned} \tag{20}$$

(b) Affine:

$$\begin{aligned} M_{ijkl}^{g,aff} &= \frac{\dot{\gamma}_0}{m} \sum_\alpha \left(\frac{\tau^\alpha}{\tau_{cr}^\alpha} \right)^{\frac{1}{m}-1} \frac{P_{ij}^\alpha P_{kl}^\alpha}{\tau_{cr}^\alpha} \\ d_{0ij}^{g,aff} &= (1 - 1/m) d_{ij}^g \end{aligned} \tag{21}$$

(c) Tangent:

With the aid of the tangent-secant relation: $\bar{\mathbf{M}}^{tg} = \bar{\mathbf{M}}^{\text{sec}}/m$ (Hutchinson, 1976), the tangent scheme gives the interaction tensor:

$$\tilde{\mathbf{M}}^{g} = (\mathbf{I} - \mathbf{S}^{g})^{-1} : \mathbf{S}^{g} : \bar{\mathbf{M}}^{\text{sec}}/m \tag{22}$$

(d) m^{eff}:

The m^{eff} scheme introduces an adjustable parameter m^{eff}, such that $m < m^{eff} < 1$. The interaction tensor is therefore given by:

$$\tilde{\mathbf{M}}^{g} = (\mathbf{I} - \mathbf{S}^{g})^{-1} : \mathbf{S}^{g} : \bar{\mathbf{M}}^{\text{sec}}/m^{eff} \tag{23}$$

For details concerning the visco-plastic adaptation of the self-consistent algorithms we refer to Lebensohn and Tomé (1993).

The Predominant Twin Reorientation (PTR) scheme proposed by Tomé et al. (1991) is used in the present paper to model the twinning activities. Within each grain g, the PTR scheme tracks the shear strain $\gamma^{\alpha,g}$ contributed by each twin system α, and the associated volume fraction $V^{\alpha,g} = \frac{\gamma^{\alpha,g}}{\gamma^{tw}}$ as well; here γ^{tw} is the characteristic shear (constant) associated with twinning. The sum over all twin systems associated with a given twin mode, and then over all the grains, represents the 'accumulated twin fraction' $V^{acc,mode}$ in the aggregate for the particular twin mode:

$$V^{acc,mode} = \sum_{g} \sum_{\alpha} V^{\alpha,g} \tag{24}$$

Since it is not numerically feasible to consider each twinned fraction as a new orientation, the PTR scheme adopts a statistical approach. At each incremental step, some grains are fully reoriented by twinning provided certain conditions are fulfilled. The 'effective twinned fraction' $V^{eff,mode}$ is the volume associated with the fully reoriented grains for the mode, and a threshold volume fraction is defined as

$$V^{th,mode} = A^{th1} + A^{th2} \frac{V^{eff,mode}}{V^{acc,mode}} \tag{25}$$

where A^{th1} and A^{th2} are two material constants. After each deformation increment a grain is randomly selected and the twin system with the highest accumulated volume fraction is identified. If the latter is larger than the threshold $V^{th,mode}$ the grain is allowed to reorient, and $V^{eff,mode}$ and $V^{acc,mode}$ are updated accordingly. The process is repeated until either all grains are checked or the effective twin volume exceeds the accumulated twin volume. In the latter case reorientation by twinning is ceased and the next deformation step is considered. Two things are

achieved in this process: a) only the historically most active twin system in each grain is considered for reorienting the whole grain by twinning, and b) the twinned fraction is consistent with the shear activity that the twins contribute to deformation.

For simplicity, the VPSC models with Affine, Secant, Tangent and m^{eff} SCSs are respectively referred to as the Affine, Secant, Tangent and m^{eff}=0.1 (meff=0.1 in figure legends) models in the remainder of this paper.

4 Results and Discussion

Various polycrystal plasticity models including the classical full-constrained Taylor model and VPSC model with various SCSs are applied to simulate large strain uniform simple shear and large strain fixed-end torsion of circular solid bars. In order to study the effects of initial texture on simple shear and torsion, we consider a random texture and a typical extrusion texture. Both initial textures are represented by 1200 orientations and are shown in Fig. 2 in terms of $\{0001\}$ and $\{10\bar{1}0\}$ pole figures in θ - $z\,(e_2-e_3)$and r-θ (e_1-e_2) planes. It has been generally accepted that the predicted second-order normal stress is sensitive to the initial texture and its symmetries (see e.g. Harren et al., 1989). Theoretically, in the absence of certain symmetries, the initial developments in the normal stress can actually be attributed, to some extent, to these 'initial textures' which do not satisfy the sample symmetries. The initial textures considered in the present paper have 1200 grains/orientations. They are constructed from orientation distributions with 300 grains by symmetrizing them with respect to the z-axis and θ - z plane. Consequently, these two initial textures are axisymmetric about the z-axis (see Fig. 2b) and symmetric about the r-θ plane (see Fig. 2a). Numerical tests indicated that the calculated shear stress components $\sigma_{r\theta}$ and σ_{rz} are nearly zero under simple shear in the θ - z plane. This implies that the initial textures reasonably satisfy the sample symmetries.

The plastic deformation in HCP materials is assumed to be resulted from slip in the Basal $\langle a\rangle$ ($\{0001\}\langle 11\bar{2}0\rangle$), Prismatic $\langle a\rangle$ ($\{10\bar{1}0\}\langle 11\bar{2}0\rangle$) and Pyramidal $\langle c+a\rangle$ ($\{\bar{1}\bar{1}22\}\langle \bar{1}\bar{1}23\rangle$) slip systems, and twinning on the $\{10\bar{1}2\}\langle \bar{1}011\rangle$ tensile twin system. Secondary twinning (twinning within already twinned parts of grains) is not considered. The reference slip/twinning rate $\dot{\gamma}_0$ and rate sensitivity$m$ are assumed to be the same for all slip/twinning systems, and are taken as $\dot{\gamma}_0 = 0.001\ s^{-1}$ and $m = 0.05$, respectively. We further assume that there are no latent hardening effects between slip systems, i.e., q_{ij}=1 (i=1, basal slip; i=2, prismatic slip; i=3, pyramidal slip). Values of the other material parameters in the Taylor model and VPSC model with various SCSs are taken from Wang et al. (2010b) and are listed in Table 1. It should be noted that q_{i4} represents the latent hardening effect between a slip/twining system (i=4, tensile twinning) and the twining system. It is important

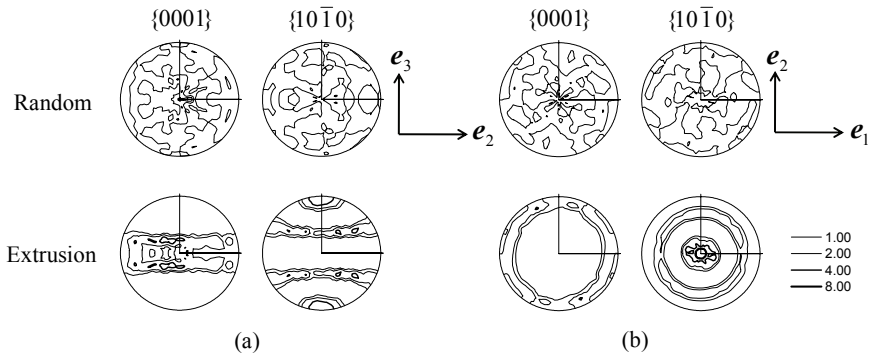

Figure 2: Initial textures represented in terms of $\{0001\}$ and $\{10\bar{1}0\}$ pole figures in (a) θ - z $(e_2 - e_3)$ plane, and (b) r-θ $(e_1 - e_2)$ plane.

to point out that the values of the material parameters for the Taylor model and Secant models are the same. It has been found that the predictions of these two models are almost the same for all deformation processes studied in Wang et al. (2010b). Figs. 3 and 4 present the uniaxial tensile stress and strain curves along the axial direction for the initial random and extrusion textures, respectively. Generally speaking, all the models show roughly the same response to uniaxial tension for both the initial random and extrusion textures. The Taylor model and Secant model give virtually the same results. Noticeable differences are that the Taylor and Secant models are above the other models when $\varepsilon < 0.06$ for the initial random texture and $\varepsilon < 0.12$ for the initial extrusion texture. At large strains, the Tangent model exhibits higher hardening.

The predicted shear stress $\tau = \sigma_{\theta z}$ and normal stress σ_{zz} as functions of the shear strain γ under simple shear in the $\theta - z$ plane, characterized by (1) with a strain rate $\dot{\gamma} = 0.001\ s^{-1}$ for the initial random texture, are presented in Fig. 5. For the shear stress response, the Taylor and Secant are very close to each other throughout the entire deformation process. At small strains, $\gamma < 0.1$, the Taylor and Secant are higher than the other models. This difference is also seen for the uniaxial results in Fig. 3. The predicted shear stress based on the Tangent shows a significantly higher hardening than the ones according to the Affine, Secant and Taylor at strains $\gamma > 0.2$. A noticeable strain softening effect is detected by the Tangent model at $\gamma \approx 1.7$. The predicted second-order normal stresses are found to be very sensitive to the models employed. The Taylor and Secant are again very close to each other. The normal stress predicted by the Taylor and Secant is compressive at $\gamma < 0.15$, tensile when $0.15 < \gamma < 0.5$, and becomes compressive again for strains $\gamma > 0.5$.

Table 1: List of values of material constants for the Taylor model and VPSC model with various self-consistent schemes.

Model	Mode	τ_0	τ_1	h_0	h_1	q_{i4}	A^{th1}	A^{th1}
Taylor	Basal	13	4	5000	30	4	0.82	0
	Prismatic	73	35	400	60	4		
	Pyramidal	110	83	2500	0	2		
	Tensile	31	0	0	0	4		
	Twin							
Affine	Basal	6	1	5000	50	4	0.7	0
	Prismatic	77	38	590	60	4		
	Pyramidal	95	100	6000	0	2		
	Tensile	50	0	0	0	4		
	Twin							
Secant	Basal	13	4	5000	30	4	0.82	0
	Prismatic	73	35	400	60	4		
	Pyramidal	110	83	2500	0	2		
	Tensile	31	0	0	0	4		
	Twin							
m^{eff}=0.1	Basal	17	6	3800	100	4	0.81	0
	Prismatic	77	33	650	50	4		
	Pyramidal	148	35	9600	0	2		
	Tensile	33	0	0	0	4		
	Twin							
Tangent	Basal	21	5	3000	140	4	0.81	0
	Prismatic	90	15	580	70	4		
	Pyramidal	145	30	9600	0	2		
	Tensile	38	0	0	0	4		
	Twin							

The Affine, m^{eff}=0.1 and Tangent all show a tensile normal stress when the deformation is small. The predicted normal stress based on the Affine model becomes compressive at $\gamma \approx 0.35$, reaches its maximum at $\gamma \approx 1.0$, and then gradually decreases. At $\gamma = 3.0$ the predicted normal stress according to the Affine model is almost zero. For the m^{eff}=0.1 and Tangent models, the early developed tensile normal stress becomes compressive at $\gamma \approx 0.25$, and then reaches its maximum at $\gamma \approx 1.0$. After that, the compressive normal stress monotonically increases based on the Tangent model. The compressive normal stress based on the m^{eff}=0.1 model gradually decreases and becomes tensile when $\gamma > 2.0$. It is interesting to note that

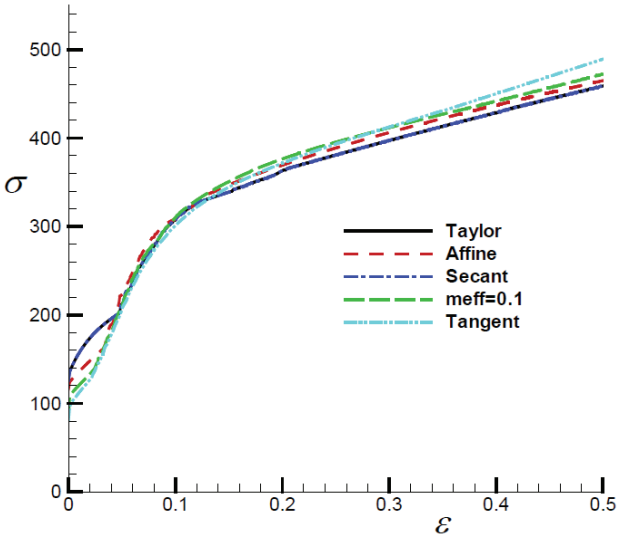

Figure 3: Predicted uniaxial stress and strain curves based on various polycrystal plasticity models for the initial random texture.

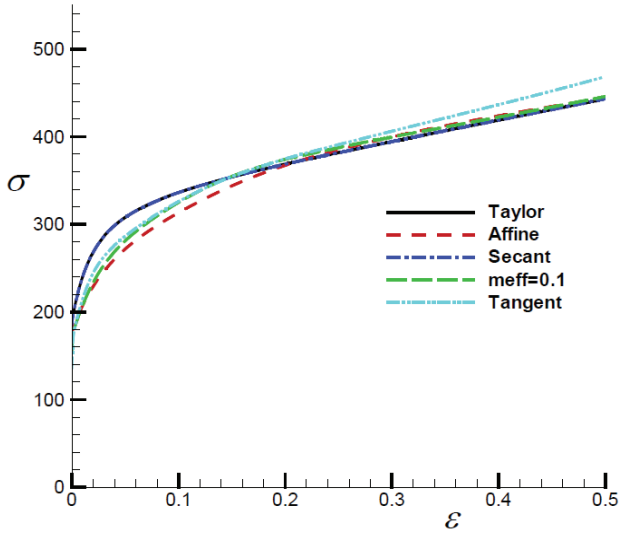

Figure 4: Predicted uniaxial stress and strain curves based on various polycrystal plasticity models for the initial extrusion texture.

the predicted normal stresses are reasonably small for all models except the Tangent model, which shows a significant softening effect in the predicted τ and γ curve at large shears.

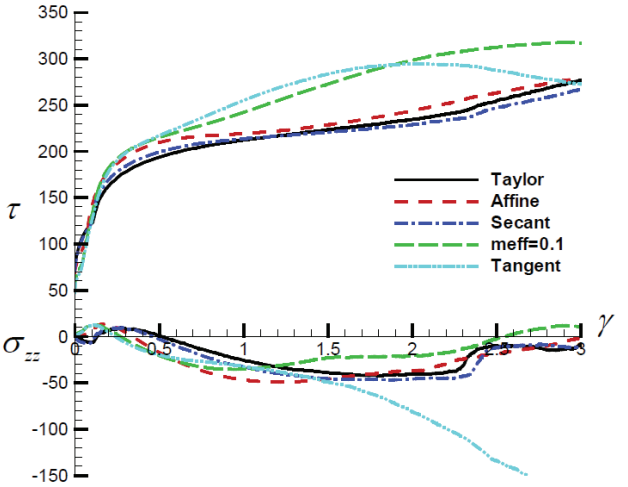

Figure 5: Predicted shear stress $\tau = \sigma_{\theta z}$ and normal stress σ_{zz} as functions of shear strain γ under simple shear for the initial random texture.

Figure 6 shows the predicted shear stress $\tau = \sigma_{\theta z}$ and normal stress σ_{zz} as functions of the shear strain γunder simple shear for the initial extrusion texture. The Taylor and Secant are very similar for both shear stress and normal stress. There is no significant softening effect in the τ and γ curve based on the Tangent model. Perhaps, the most striking difference between the initial random and extrusion textures is that much larger tensile normal stress is found for the initial extrusion texture. The normal stresses predicted by the Taylor, Secant and Affine are almost always tensile. By contrast, the predicted normal stress becomes compressive when $\gamma > 0.6$ and 0.9 for the Tangent and m^{eff}=0.1 models, respectively. Furthermore, the predicted compressive normal stress at large shears is much larger in the Tangent model than in the m^{eff}=0.1 model.

The differences in the predicted stress responses between the various models shown in Figs. 5 and 6 may result from different slip/twinning activities in these models. Figs. 7 and 8 present relative activities of slip/twinning under simple shear for the initial random and extrusion textures, respectively. It is found that slip/twinning activities in the Taylor and Secant models are very similar for both initial textures. For the initial random texture, twinning activity is noticeable only at very small shears.

A close observation reveals that twinning is relatively more active in the Affine, Tangent and m^{eff}=0.1 than in the Taylor and Secant models. In the m^{eff}=0.1 and Tangent models, Basal slip is the most important slip/twinning activity when shear is very small and becomes less important at large strains when Pyramidal slip is more and more active. The predicted slip/twinning activities are very similar in the Taylor, Secant and Affine models. More specifically, Basal slip activity is an important contribution to plastic deformation during the entire deformation process, while Pyramidal slip is more active when Prismatic slip activity gradually decreases with increasing shear. It is important to note that Pyramidal slip becomes dominant at large shears in the Tangent model, which may be related to the extremely high compressive normal stress shown in Fig. 5.

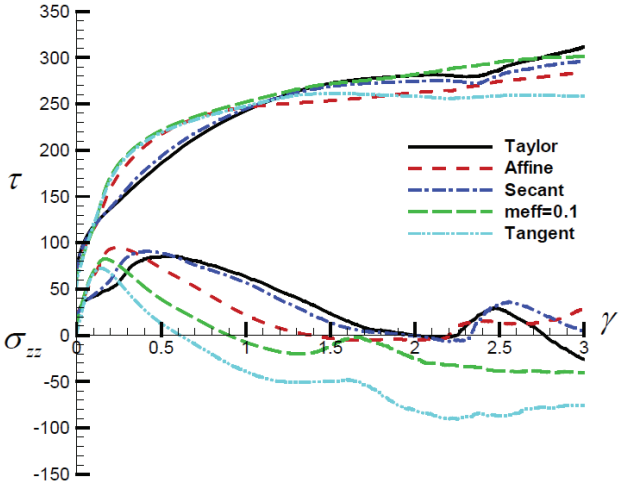

Figure 6: Predicted shear stress $\tau = \sigma_{\theta z}$ and normal stress σ_{zz} as functions of shear strain γ under simple shear for the initial extrusion texture.

The twinning activity under simple shear for the initial extrusion texture is significantly less than for the initial random texture at very small shear strains. The small but noticeable second twinning is found at $\gamma \approx 2.2$ for the Taylor, Secant and Affine models. The predicted trends for activities of Basal, Prismatic and Pyramidal slip systems are somewhat similar to those for the initial random texture. The most important difference is that Basal slip activity decreases very rapidly in the m^{eff}=0.1 and Tangent models. In the Taylor, Secant and Affine models, Pyramidal slip is considerably more active than Basal slip when $\gamma > 0.7$, while these two activities are roughly at the same level for the initial random texture. Once again, Pyramidal slip becomes dominant in the Tangent model at large strains, where large compres-

sive normal stress is predicted (see Fig. 6). Furthermore, Prismatic slip system is noticeably more active under simple shear for the initial extrusion texture than for the initial random texture when $\gamma < 0.75$. It is noted that within this strain range the predicted normal stress is tensile and large.

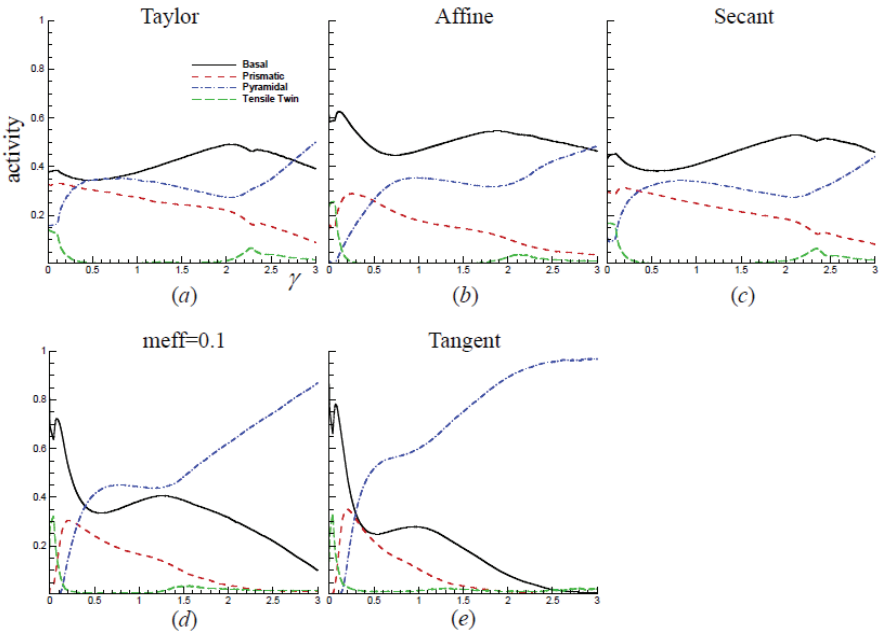

Figure 7: Predicted slip/twinning activities for the initial random texture under simple shear based on various polycrystal plasticity models.

Figures 9 and 10 show the predicted deformation textures under simple shear at a shear strain $\gamma = 1$ for the initial random texture and extrusion texture, respectively. All the models exhibit shear textures analogous to the experimental textures observed in simple shear by Beausir et al. (2007) and in free-end torsion by Beausir et al. 2009) for HCP materials. Closer examination reveals that the Taylor and Secant models are very close, while the deformed textures based on the Affine, m^{eff}=0.1 and Tangent are very similar.

The development of the second-order normal stress is believed to mainly result from the initial and deformation induced anisotropy and is thus sensitive to the texture evolution. Figs. 11 and 12 give the predicted shear stress $\tau = \sigma_{\theta z}$ and normal stress σ_{zz} as functions of the shear strain γ under simple shear for the initial random texture and extrusion texture, respectively. In these simulations texture evolution

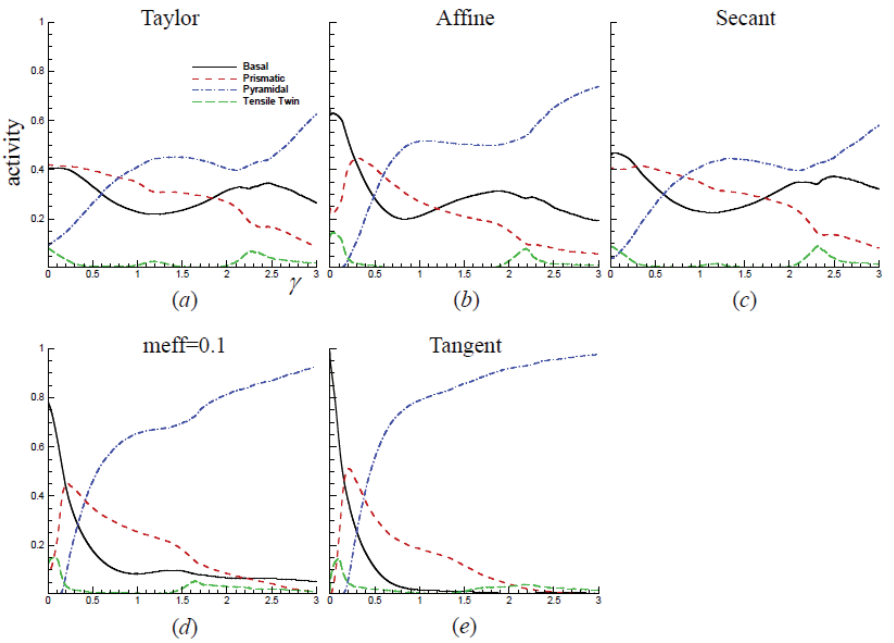

Figure 8: Predicted slip/twinning activities for the initial extrusion texture under simple shear based on various polycrystal plasticity models.

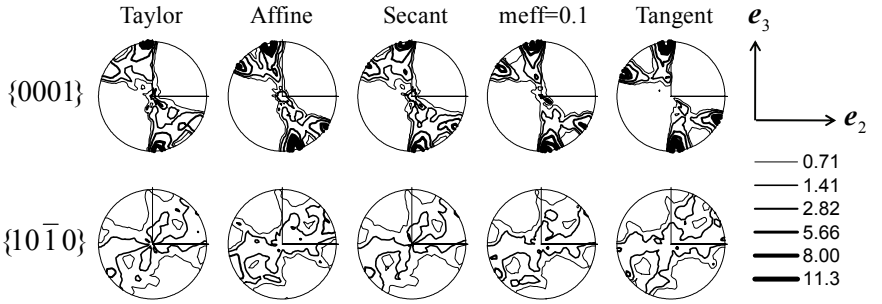

Figure 9: Predicted deformation textures under simple shear at shear strain $\gamma = 1$ for the initial random texture.

is excluded. It is important to point out that in these simulations both texture evolution due to slip and reorientation due to twinning are excluded. It is found that excluding texture evolution dramatically reduces the predicted normal stress for all the models. For the initial random texture, the predicted normal stresses are

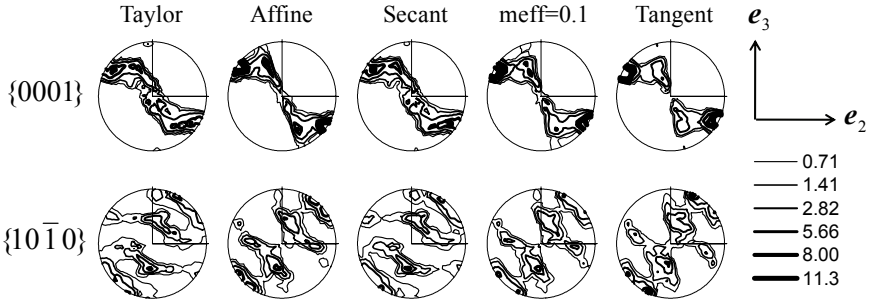

Figure 10: Predicted deformation textures under simple shear at shear strain $\gamma = 1$ for the initial extrusion texture.

nearly zero during the entire deformation process. The corresponding predicted slip/twinning activities are shown in Figs. 13 and 14 for the initial random texture and extrusion texture, respectively. For the initial random texture and with respect to the cases with texture evolution, excluding texture evolution results in: (I) a monotonic reduction of the Basal slip activities in all the models especially in the m^{eff}=0.1 and Tangent models, where a very rapid reduction is found; (II) noticeably active Prismatic slip; and (III) more active Pyramidal slip in the Taylor, Secant and Affine models at large shears. For the initial extrusion texture and with respect to the cases with texture evolution, excluding texture evolution results in: (I) a monotonic decrease of the Basal slip activities; (II) more active Prismatic slip especially at large strains; and (III) less active Pyramidal slip in the Taylor, Secant and Tangent models, and much less active in the Affine and m^{eff}=0.1 models, at large shears. For both initial textures, the twinning activity is noticeable only at very small shears. The predicted volume fractions of twinned regions for the initial extrusion texture with and without texture evolution are presented in Fig. 15. It is found that all the models show roughly the same trend. It is also observed that texture evolution makes twinning more difficult to occur.

We now proceed to study the large strain fixed-end torsion of a circular solid bar. As mentioned previously, each material point in the circular solid bar is simply loaded in simple shear under an additional hydrostatic pressure, where the shear strain γ is directly proportional to the radius r. Thus, the simple shear results reported above can be extended to the analysis of the fixed-end torsion of the circular solid bar using the semi-analytical approach developed by Neale and Shrivastava (1985) and recapped in Section 2. Figs. 16 and 17 show the predicted mean shear stress $\bar{\tau}$ and mean axial stress $\bar{\sigma}$ as functions of the shear strain Γ at the outer radius of the bar under fixed-end torsion for the initial random and extrusion textures,

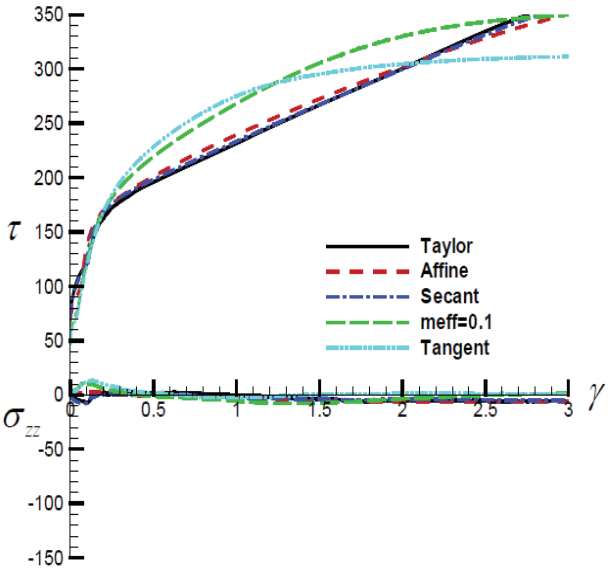

Figure 11: Predicted shear stress $\tau = \sigma_{\theta z}$ and normal stress σ_{zz} as functions of shear strain γ under simple shear for the initial random texture. Texture evolution is excluded.

respectively. It is clear that the predicted torsional responses are much smoother than the corresponding simple shear results, especially at large strains. For the initial random texture, the predicted mean axial stress $\bar{\sigma}$ is compressive at large strains for all the models. Furthermore, the softening effect in the τ vs. γ curve under simple shear predicted by the Tangent model (Fig. 5) is significantly reduced in the $\bar{\tau}$ vs. Γ curve under fixed-end torsion. It is expected that the solid bar may elongate axially if the axial constraint is removed; i.e., under free-end torsion. For the initial extrusion texture, the Taylor, Secant and Affine models predict tensile mean axial stresses during the entire deformation process. The calculated mean axial stresses are tensile at small strains and become compressive when $\Gamma > 1.5$ and 1.0 for the m^{eff}=0.1 and Tangent models, respectively. This may imply that a solid bar with the initial extrusion texture under free-end torsion shortens in the axial direction based on the Taylor, Secant and Affine models. However, the predicted axial response under free-end torsion based on the m^{eff}=0.1 and Tangent models may exhibit a complicated trend: contracting first and then elongating axially. It is important to note that Beausir et al. (2009) have investigated the free-end torsion for magnesium alloy AZ71 at various temperatures and strain rates. They found that, within the shear strain range of $\Gamma < 0.8$, axial contraction occurs in all the

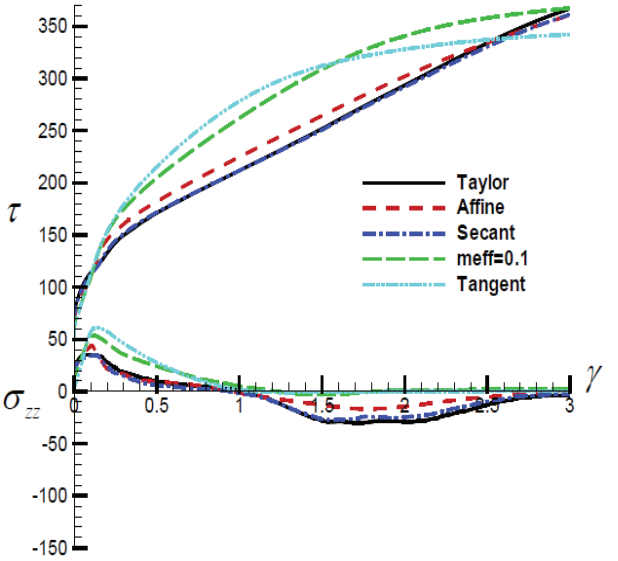

Figure 12: Predicted shear stress $\tau = \sigma_{\theta z}$ and normal stress σ_{zz} as functions of shear strain γ under simple shear for the initial extrusion texture. Texture evolution is excluded.

cases examined. The predicted $\bar{\sigma}$ vs. Γ curve under fixed-end torsion shown in Fig. 17 seems in a good qualitative agreement with the experimental axial strain vs. Γ curve under free-end torsion reported by Beausir et al. (2009).

Based on the simple shear results reported previously, it is expected that texture evolution has a significant influence on the predicted torsional response. The effects of texture evolution on the predicted mean shear stress $\bar{\tau}$ and mean axial stress $\bar{\sigma}$ as functions of the shear strain Γ at the outer radius of the circular solid bar under fixed-end torsion for the initial random and extrusion textures are respectively presented in Figs. 18 and 19. Texture evolution is excluded in these simulations. It is observed that the second-order mean axial stress is dramatically reduced for both initial textures and for all the models employed. For the initial random texture, the predicted axial stress remains very small. For the initial extrusion texture, when the strains are not very large all the models give a tensile mean axial stress. At large strains, the mean axial stresses predicted by the m^{eff}=0.1 and Tangent models remain tensile although small, while compressive mean axial stresses are calculated from the Taylor, Secant and Affine models. These observations are opposite to what was found in the cases where texture evolution is accounted for (see Fig. 17).

Finally, it is worth mentioning that the polycrystal plasticity models employed in

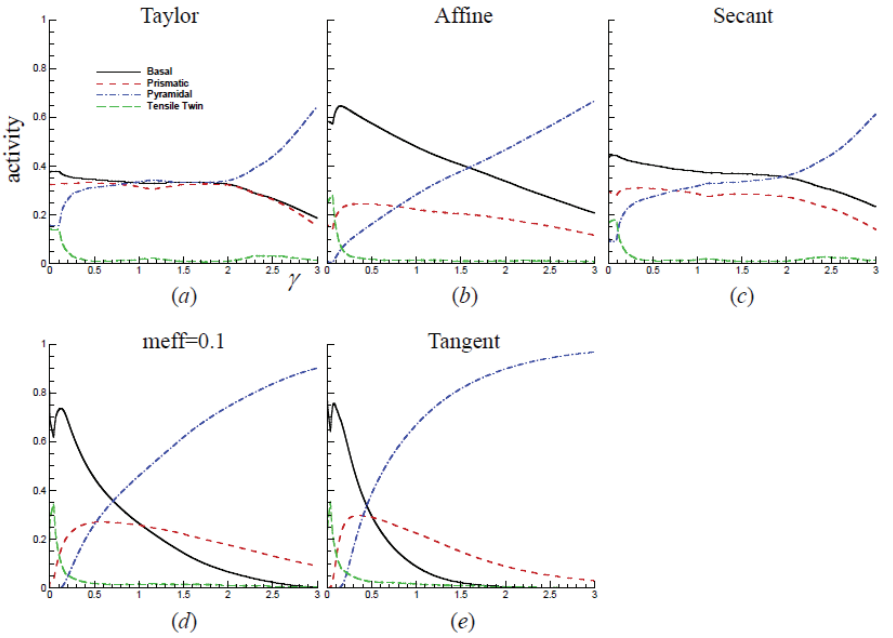

Figure 13: Predicted slip/twinning activities for the initial random texture under simple shear based on various polycrystal plasticity models.

the present study are such that a superimposed hydrostatic pressure has no effect on the predicted textures. Furthermore, each element of the solid bar in torsion is in a state of simple shear under an additional hydrostatic pressure. Therefore, deformed textures under simple shear are sufficient to describe the texture evolution throughout the solid bar.

5 Conclusions

In this paper, the large strain uniform simple shear of Hexagonal Close Packed (HCP) polycrystals has been first studied numerically, based on the classical Taylor model and the Visco-Plastic Self-Consistent (VPSC) model with various self-consistent schemes. In these polycrystal plasticity models, both slip and twinning contribute to plastic deformation. The simple shear results have been extended to the large strain fixed-end torsion of solid circular bars.

It has been found that the development of the second-order normal stress in fixed-end torsion is very sensitive to the initial anisotropy due to the initial texture, and the deformation induced anisotropy due to the texture evolution. Numerical re-

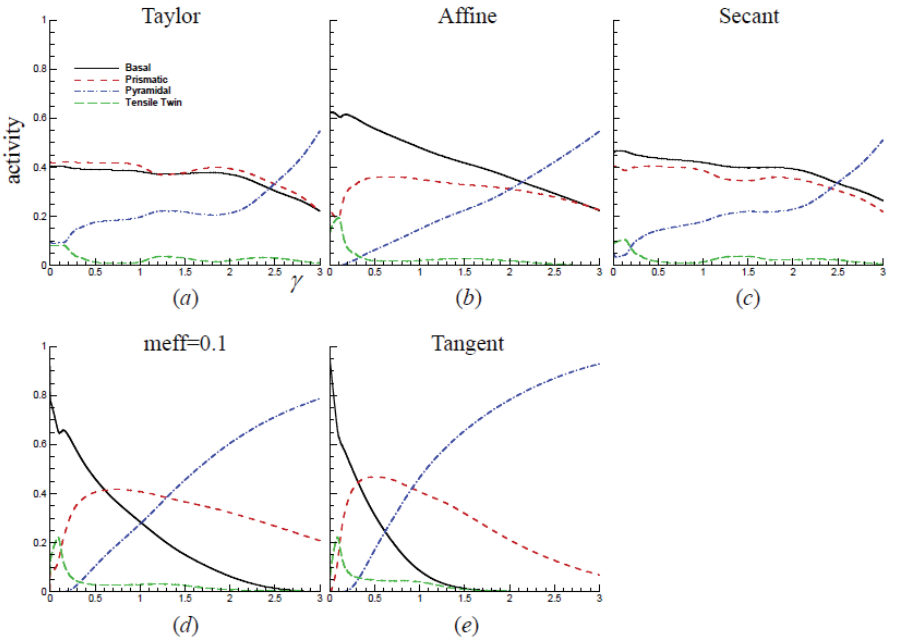

Figure 14: Predicted slip/twinning activities for the initial extrusion texture under simple shear based on various polycrystal plasticity models. Texture evolution is excluded.

sults have indicated that excluding texture evolution dramatically reduces the development of the axial force. It has been also observed that the predicted normal force depends strongly on the polycrystal plasticity models employed. For the extruded solid bars, the Taylor, Secant and Affine models predict tensile normal forces throughout the deformation process, while the m^{eff}=0.1 and Tangent models show tensile normal forces at relatively small strains and compressive normal stresses at large strains. These findings imply that the torsion test can provide an effective means for assessing the adequacy of constitutive models. Therefore, the polycrystal plasticity models for HCP materials considered in the present paper can be efficiently evaluated when experimental data for fixed-end torsion of HCP polycrystals become available.

Finally, it is worth mentioning that the Crystal Plasticity Finite Element Model (CPFEM) has also been applied to study the large strain behavior of HCP polycrystals (see e.g. Mayama et al., 2009; Choi et al., 2010). In CPFEM simulations an element of the FE mesh represents either a single crystal or a part of a single crystal, and the constitutive response at an integration point is described by the single

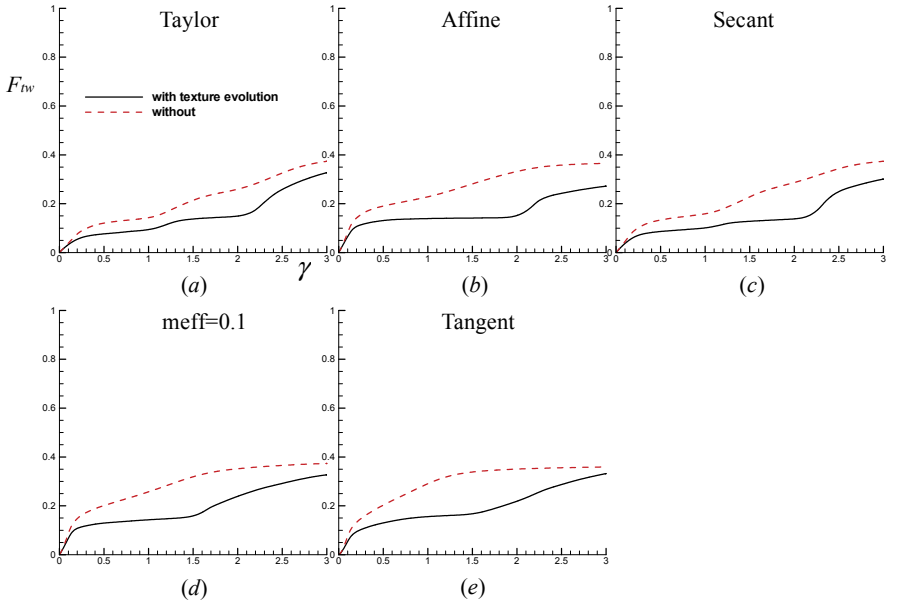

Figure 15: Predicted volume fractions of twinned regions for the initial extrusion texture with and without texture evolution.

crystal constitutive model. This approach enforces both equilibrium and compatibility throughout the polycrystalline aggregate in the weak FE sense (Anand and Kalidindi, 1994; Wu et al., 2004). Furthermore, it facilitates consideration of grain morphology and the modeling of localized deformations in single and polycrystals (Wu et al., 2007b; Shi et al., 2010). However, this method is computationally much more intensive than the polycrystal plasticity models.

Acknowledgement: H. Wang and P.D. Wu were supported by funding from the NSERC Magnesium Strategic Research Network. More information on the Network can be found at www.MagNET.ubc.ca. Y. Wu was supported by the National Basic Research Program of China (2007CB209400) and the 111 Project of China (B07028).

References

Agnew, S.R.; Duygulu, O. (2005): Plastic anisotropy and the role of non-basal slip in magnesium alloy AZ31B. *Int. J. Plasticity*, vol. **21**, pp.1161–1193.

Anand, L.; Kalidindi, S.R. (1994): The process of shear-band formation in plane-

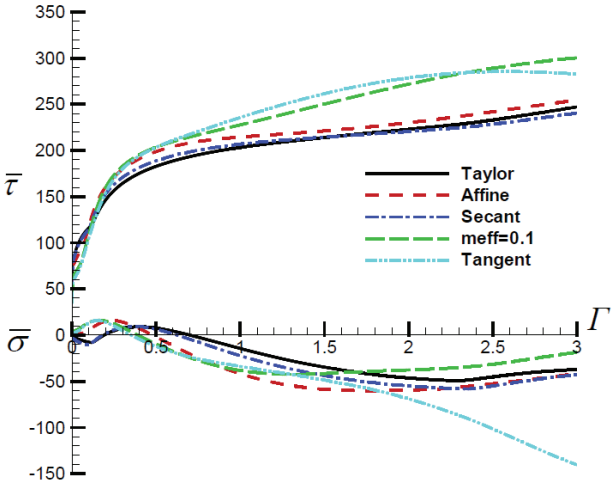

Figure 16: Predicted mean shear stress $\bar{\tau}$ and mean axial stress $\bar{\sigma}$ as functions of the shear strain Γ at the outer radius of the circular solid bar with the initial random texture under fixed-end torsion.

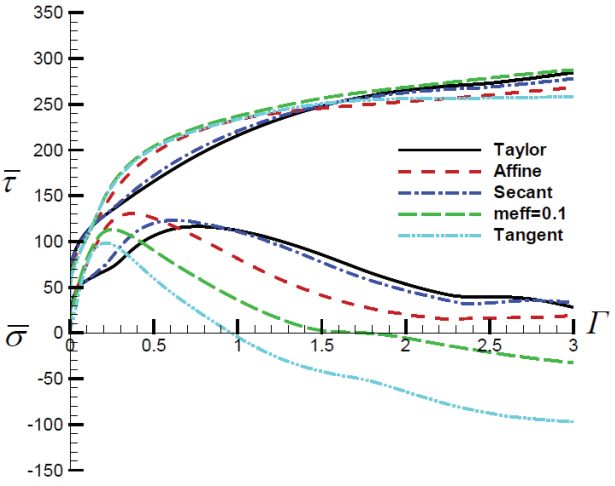

Figure 17: Predicted mean shear stress $\bar{\tau}$ and mean axial stress $\bar{\sigma}$ as functions of the shear strain Γ at the outer radius of the circular solid bar with the initial extrusion texture under fixed-end torsion.

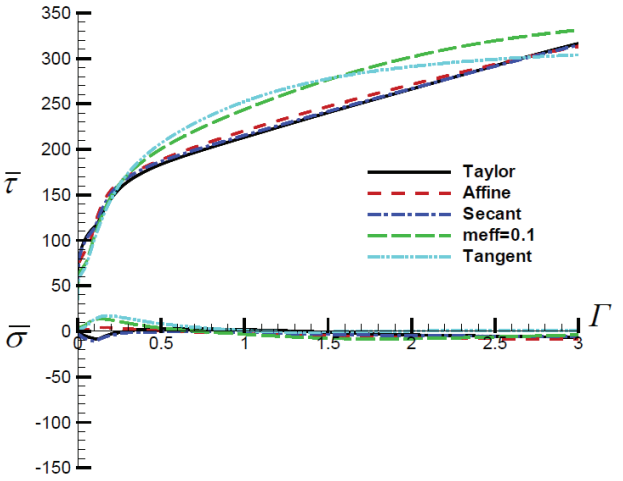

Figure 18: Predicted mean shear stress $\bar{\tau}$ and mean axial stress $\bar{\sigma}$ as functions of the shear strain Γ at the outer radius of the circular solid bar with the initial random texture under fixed-end torsion. Texture evolution is excluded.

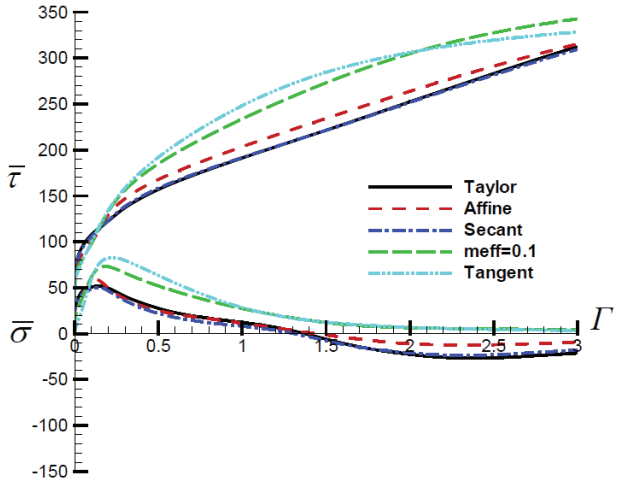

Figure 19: Predicted mean shear stress $\bar{\tau}$ and mean axial stress $\bar{\sigma}$ as functions of the shear strain Γ at the outer radius of the circular solid bar with the initial extrusion texture under fixed-end torsion. Texture evolution is excluded.

strain compression of FCC metals - effects of crystallographic texture. *Mech. Mater.*, vol. **17**, pp. 223–243.

Asaro, R.J.; Needleman, A. (1985): Texture development and strain hardening in rate dependent polycrystals. *Acta Metall. Mater.*, vol. **33**, pp.923–953.

Balasubramanian, S.; Anand, L. (2002): Plasticity of initially textured hexagonal polycrystals at high homologous temperatures: application to titanium. *Acta Mater.,* vol. **50**, pp.133–148.

Barnett, M.R. (2001): Influence of deformation condition and texture on the high temperature flow stress of magnesium AZ31. *J. Light Met.*, vol.**1**, pp. 167–177.

Beausir, B.; Toth, L.S.; Neale, K.W. (2007): Ideal orientations and persistence characteristics of hexagonal close packed crystals in simple shear. *Acta Mater.*, vol. **55**, pp. 2695–2705.

Beausir, B.; Toth, L.S.; Qods, F.; Neale, K.W. (2009): Texture and mechanical behavior of magnesium during free-end torsion. *J. Eng. Mater. Technol.*, vol. **131**, article number 011108.

Billington, E.W. (1977): Non-linear response of various metals: II. Permanent length changes in twisted tubes. *J. Phys. D: Appl. Phys.,* vol. **10**, pp. 533–552.

Choi, S.H.; Kim, D.H.; Park, S.S.; You, B.S. (2010): Simulation of stress concentration in Mg alloys using the crystal plasticity finite element method. *Acta Mater.*, vol. **58**, pp. 320–329.

Dawson, P.R.; MacEwen, S.R.; Wu, P.D. (2003): Advances in sheet metal forming analyses: dealing with mechanical anisotropy from crystallographic texture. *Int. Mater. Rev.*, vol. **48**, pp. 86–122.

Eshelby, J.D. (1957): The determination of the elastic field of an ellipsoidal inclusion, and related problems. *P. R. Soc.*, vol. **A241**, pp. 376–396.

Evans, W.J.; Jones, J.P.; Whittaker, M.T. (2005): Texture effects under tension and torsion loading conditions in titanium alloys. *Int. J. Fatigue*, vol. **27**, pp. 1244–1250.

Field, D.P.; Adams, B.L. (1990): Unrecoverable strain hardening in torsionally strained OFHC copper. *J. Eng. Mater. Technol.*, vol. **112**, pp. 315–320.

Harren, S.; Lowe, T.C.; Asaro, R.J.; Needleman, A. (1989): Analysis of large-strain shear in rate-dependent Face-Centred Cubic polycrystals: Correlation of micro- and macromechanics. *Philos. T. R. Soc. Lond.,* vol. **A328**, pp. 443–500.

Hutchinson, J.W. (1976): Bounds and self-consistent estimates for creep of polycrystalline materials. *P. R. Soc.,* vol. **A348**, pp. 101–127.

Jain, A.; Agnew, S.R. (2007): Modeling the temperature dependent effect of twin-

ning on the behavior of magnesium alloy AZ31B sheet. *Mater. Sci. Eng.*, vol. **A462**, pp. 29–36.

Kalidindi, S.R. (1998): Incorporation of deformation twinning in crystal plasticity models. *J. Mech. Phys. Solids*, vol. **46**, pp. 267–290.

Khen, R.; Rubin, M.B. (1992): Analytical modelling of second order effects in large deformation plasticity *Int. J. Solids Struct.*, vol. **29**, pp. 2235–2258.

Kröner, E. (1958): Berechnug der elastischen konstanten des vielkristalls aus den konstanten des einnkristalls. *Z. Phys.*, vol. **151**, pp. 504–518.

Lebensohn, R.A.; Tomé, C.N. (1993): A self-consistent anisotropic approach for the simulation of plastic deformation and texture development of polycrystals - Application to zirconium alloys. *Acta Metall. Mater.*, vol. **41**, pp. 2611–2624.

Lebensohn, R.A.; Tomé, C.N. (1994): A self-consistent viscoplastic model - Prediction of rolling textures of anisotropic polycrystals. *Mater. Sci. Eng.*, vol. **A175**, pp. 71–82.

Masson, R.; Bornert, M.; Suquet, P.; Zaoui, A. (2000): An affine formulation for the prediction of the effective properties of nonlinear composites and polycrystals. *J. Mech. Phys. Solids*, vol. **48**, pp. 1203–1227.

Mayma, T.; Aizawa, K.; Tadano, Y.; Kuroda, M. (2009): Influence of twinning deformation and lattice rotation on strength differential effect in polycrystalline pure magnesium with rolling texture. *Comput. Mater. Sci.*, vol. **47**, pp. 448–455.

Molinari, A.; Canova, G.R.; Ahzi, S. (1987): A self-consistent approach of the large deformation polycrystal viscoplasticity. *Acta Metall.*, vol. **35**, pp. 2983–2994.

Montheillet, F.; Cohen, M.; Jonas, J.J. (1984): Axial stresses and texture development during the torsion testing of Al, Cu and Alpha-Fe. *Acta Metall.*, vol. **32**, pp. 2077–2089.

Neale, K.W.; Shrivastava, S.C. (1985): Finite elastic plastic torsion of a circular bar. *Eng. Fract. Mech.*, vol. **21**, pp. 747–754.

Neale, K.W.; Shrivastava, S.C. (1990): Analytical solutions for circular bars subjected to large strain plastic torsion. *J. Appl. Mech.*, vol. **57**, pp. 298–306.

Neale, K.W.; Toth, L.S.; Jonas, J.J. (1990): Large strain shear and torsion of rate-sensitive FCC polycrystals. *Int. J. Plasticity*, vol. **6**, pp. 45–61.

Sanchez, P. ; Pochettino, A. ; Chauveau, T. ; Bacroix, B. (2001) : Torsion texture development of zirconium alloys. *J. Nucl. Mater.*, vol. **298**, pp. 329–339.

Shi, Y.; Wu, P.D.; Lloyd, D.J.; Embury, J.D. (2010): Crystal plasticity based analysis of localized necking in aluminum tube under internal pressure. *Eur. J.*

Mech. A-Solid., vol. **29**, pp. 475–483.

Staroselsky, A.; Anand, L. (1998): Inelastic deformation of F.C.C. materials by slip and twinning. *J. Mech. Phys. Solids*, vol. **46**, pp. 671–696.

Staroselsky, A.; Anand, L. (2003): A constitutive model for hcp materials deforming by slip and twinning: application to magnesium alloy AZ31B. *Int. J. Plasticity*, vol. **19**, pp. 1853–1864.

Swift, H.W. (1947): Length changes in metals under torsional overstrain. *Engineering*, vol. **163**, pp. 253–257.

Taylor, G.I. (1938): Plastic strain in metals. *J. Inst. Metals,* vol. **62**, pp. 307–324.

Toth, L.S.; Jonas, J.J.; Daniel, D.; Bailey, J.A. (1992): Texture development and length changes in copper bars subjected to free end torsion. *Texture Microstruct.*, vol. **19**, pp. 245–262.

Tomé, C.N.; Lebensohn, R.A.; Kocks, U.F. (1991): A model for texture development dominated by deformation twinning - Application to zirconium alloys. *Acta Metall. Mater.*, vol. **39**, pp. 2667–2680.

Wang, H.; Wu, P.D.; Tomé, C.N.; Huang, Y. (2010a): A finite strain elastic-viscoplastic self-consistent model for polycrystalline materials. *J. Mech. Phys. Solids*, vol. **58**, pp. 594–612.

Wang, H.; Raeisinia, B.; Wu, P.D.; Agnew, S.R.; Tomé, C.N. (2010b): Evaluation of self-consistent crystal plasticity models for magnesium alloy AZ31B sheet. *Int. J. Solids Structures*, vol. **47**, pp. 2905–2917.

Wang, H.; Wu, P.D.; Neale, K.W. (2010c): On the role of the constitutive model and basal texture on the mechanical behavior of magnesium alloy AZ31B sheet. *J. Zhejiang Univ.-Sc. A*, vol. **11**, pp. 744–755.

Wu, X.; Kalidindi, S.R.; Necker, C.; Salem, A.A. (2007a): Prediction of crystallographic texture evolution and anisotropic stress-strain curves during large plastic strains in high purity α-titanium using a Taylor-type crystal plasticity model. *Acta Mater.,* vol. **55**, pp. 423–432.

Wu, P.D.; Lloyd, D.J. (2004): Analysis of surface roughening in AA6111 automotive sheet. *Acta Mater.*, vol. **52,** pp. 1785–1798.

Wu, P.D.; Lloyd, D.J.; Jain, M.; Neale, K.W.; Huang, Y. (2007b): Effects of spatial grain orientation distribution and initial surface topography on sheet metal necking. *Int. J. Plasticity*, vol. **23**, pp. 1084–1104.

Wu, P.D.; Neale, K.W.; Van der Giessen, E. (1996): Simulation of the behaviour of FCC polycrystals during reversed torsion. *Int. J. Plasticity*, vol. **12**, pp. 1199–1219.

Wu, P.D.; Neale, K.W.; Van der Giessen, E. (1997): On crystal plasticity FLD analysis *P. R. Soc. Lond.*, vol. **A453**, pp. 1831–1848.

Wu, P.D.; Van der Giessen, E. (1993): On large strain inelastic torsion of glassy polymers. *Int. J. Mech. Sci.*, vol. **35**, pp. 935–951.

Xu, F.; Holt, R.A.; Daymond, M.R. (2008): Modeling lattice strain evolution during uniaxial deformation of textured Zircaloy-2. *Acta Mater.*, vol. **56**, pp. 3672–3687.